Meteoritics & Planetary Science 61, Nr 7, 1386–1398 (2026)
doi: 10.1111/maps.70088

A geophysical investigation of the Roter Kamm impact crater, Namibia

Hannah NIENHAUS [1,2]*, Pritam YOGESHWAR [1,3], Wiebke MÖRBE [1,3], Bülent TEZKAN [1], Yajun LIU [4], Bufelo LUSHETILE [5], and Martin MELLES [6]

[1]Institute of Geophysics and Meteorology, University of Cologne, Cologne, Germany
[2]School of Ocean and Earth Science, University of Southampton, Southampton, UK
[3]LIAG Institute for Applied Geophysics, Hanover, Germany
[4]Badong National Observation and Research Station of Geohazards, China University of Geosciences, Wuhan, China
[5]Ministry of Mines and Energy, Geological Survey of Namibia, Windhoek, Namibia
[6]Institute of Geology and Mineralogy, University of Cologne, Cologne, Germany

***Correspondence**
Hannah Nienhaus, School of Ocean and Earth Science, University of Southampton, European Way, Southampton SO14 3ZH, UK.
Email: h.nienhaus@soton.ac.uk

(Received 02 June 2025; revision accepted 10 December 2025)

Abstract–The Roter Kamm impact crater is located in the southern Namib Desert. The crater has a diameter of 2.5 km and belongs to the category of simple, bowl-shaped impact craters, with an elevated rim of fractured target rock. The crater's interior is completely buried beneath sediments, preventing extensive surface investigations of the bedrock topography. Geophysical investigations were carried out to better characterize the sediment cover, the resulting shape of the crater, and the infill of the impact structure. Two electromagnetic techniques, transient electromagnetics and audiomagnetotellurics, were used to study the subsurface resistivity structure across and beyond the Roter Kamm crater along two transects. The postimpact sediments inside the crater reach thicknesses up to 340 m. The surface of the underlying brecciated zone exhibits the characteristic bowl-shape of a simple crater. A prominent conductive anomaly was found inside the sedimentary succession, indicating the presence of water. The boundary between fluid-saturated and dry material likely marks the transition from postimpact sediments to impact breccia. Our results provide the first geophysical model of the sedimentary infill of the Roter Kamm impact crater derived from electromagnetic methods.

INTRODUCTION

Currently, some 210 impact structures have been confirmed on Earth (Gottwald et al., 2020; Schmieder & Kring, 2020; Kenkmann, 2021; Osinski et al., 2022). The morphology of impact structures can either be simple or complex. As the name states, a complex crater represents a complex morphology with a collapsed rim section and a central uplift or central peak-ring structure, in contrast to the simple geometry of a smaller crater. In addition, a complex impact crater has a shallower depth-to-diameter ratio (Collins et al., 2012; French & Koeberl, 2010; Osinski & Pierazzo, 2013). Simple craters typically have a diameter smaller than 4 km in crystalline or 2 km in sedimentary host rock (Dence, 1972). Located in the southern Namib Desert and with a diameter of 2.5 km, Roter Kamm (cf. Figure 1a) is among the largest simple craters known on Earth. It is situated approximately 10 km west of the Aurus Mountains, which extend from southeast to northwest, indicating the general faulting direction of the region (Thomas et al., 2016).

Roter Kamm is extensively filled by eolian sand and active sand dunes, indicating that eolian activity was the dominant process in the formation of the crater infill (Miller, 2008, 2010). However, the crater rim remains largely exposed (Figure 2, Dietz, 1965; Fudali, 1973;

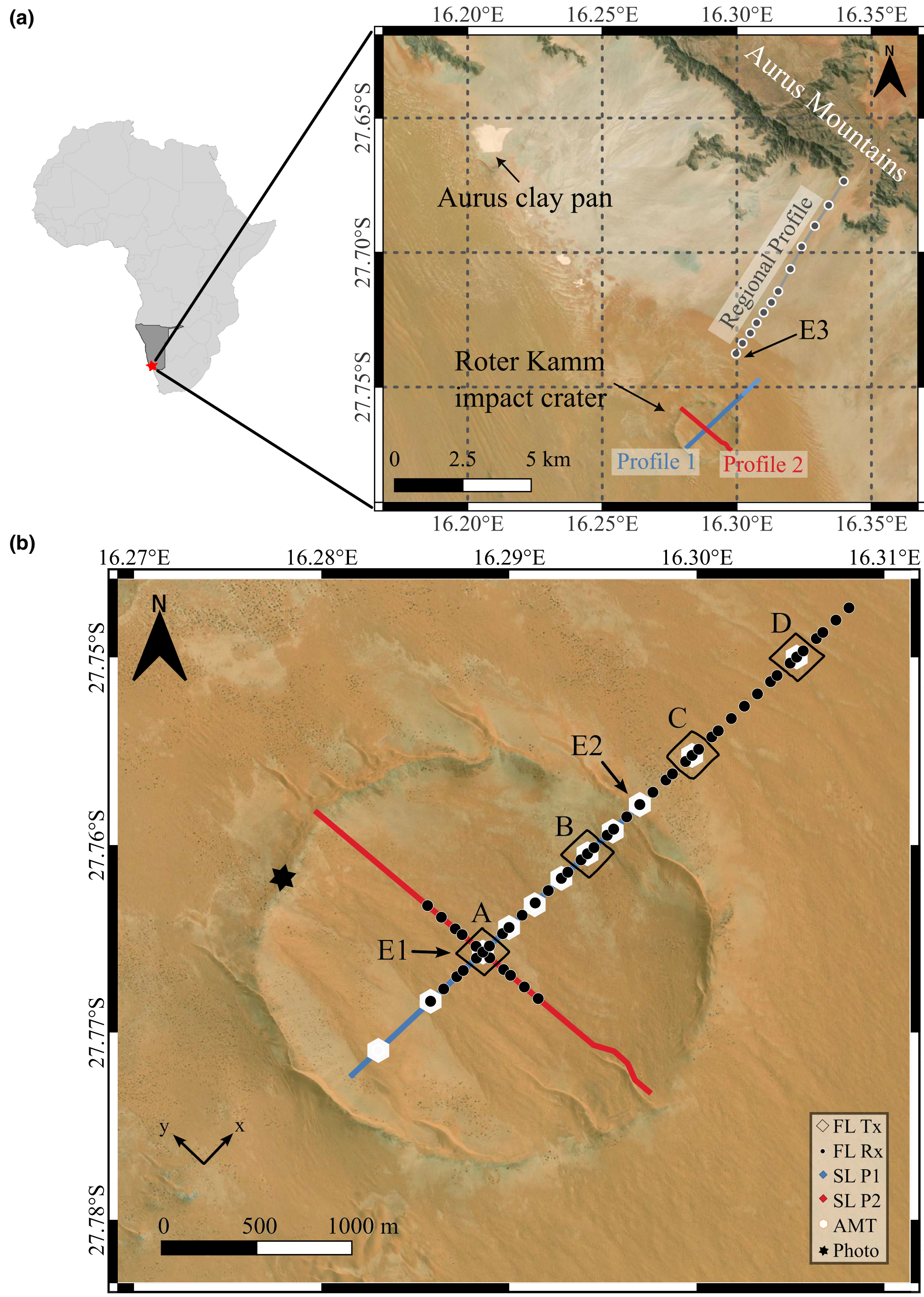

FIGURE 1. *ESRI World Imagery* basemap satellite image (Environmental Systems Research Institute [ESRI], 2022) of (a) the survey area in the Namib Desert with a map of Africa indicating Namibia (dark gray) and the location of the Roter Kamm crater (red star). (b) Close-up of the Roter Kamm impact crater with the transient electromagnetic (TEM) and audiomagnetotelluric (AMT) survey setup (Legend abbreviation: SL P1 = single-loop TEM profile 1, SL P2 = single-loop TEM profile 2, FL Tx = fixed-loop TEM transmitter (A, B, C and D), FL Rx = fixed-loop TEM receiver position, AMT = AMT sounding location). E1–E3 denote locations of interest: the crater center (E1 in b), crater rim (E2 in b), and surrounding plain (E3 in a) of the Roter Kamm. The black star marks the viewpoint from where the photograph shown is Figure 2 was taken. (Color figure can be viewed at wileyonlinelibrary.com)

Reimold & Miller, 1989; Hecht et al., 2008). Roter Kamm was formed by a meteorite impact approximately 4–5 million years ago (Hecht et al., 2008). Dietz (1965) and Fudali (1973) were the first to indicate an impact origin of the crater, but Reimold and Miller (1989) presented the first diagnostic evidence. The basement in

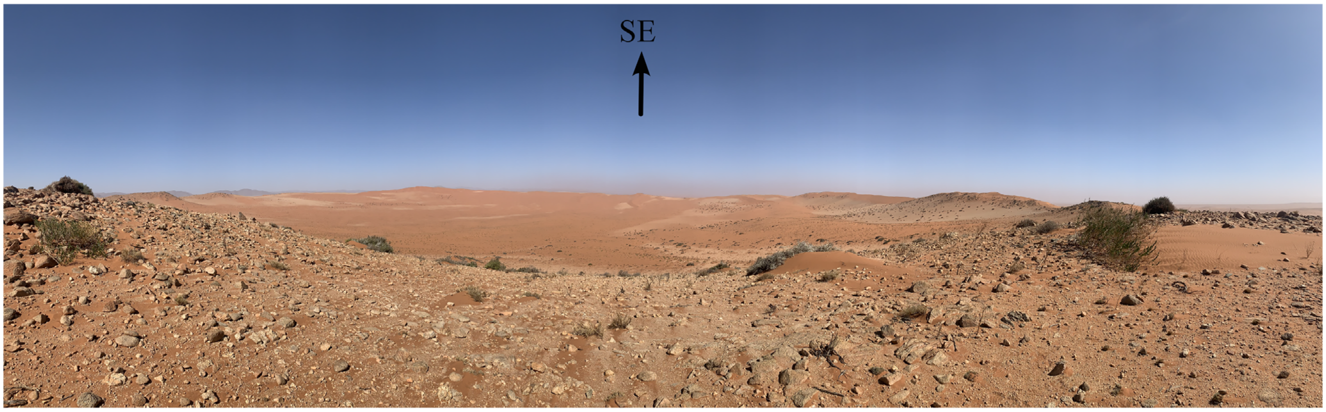

FIGURE 2. Photograph taken during the field survey from the northwestern rim of the Roter Kamm crater toward the southeast. The viewpoint from where the image was taken is marked by a black star in Figure 1b. (Color figure can be viewed at wileyonlinelibrary.com)

this area is the Namaqua Metamorphic Complex, a granitic gneiss containing quartz veins and pegmatites (cf. Koeberl, 1994; Miller, 2008; Reimold et al., 1994; Thomas et al., 2016). The basement is exposed at the crater rim, showing notable brecciation. Cataclastic breccia occurrences with radial orientation are widespread (Miller, 2008). The basement is covered by semiconsolidated sediments of the Tsondab sandstone formation, overlain by a layer of eolian sands from the Sossus sand formation (Miller, 2008; Reimold et al., 1994). The main ejecta apron is situated to the northwest of the crater (Miller, 2008; Reimold & Miller, 1989). Based on the location of the ejecta apron and the higher density of cataclastic breccia veins in the northwestern sector of the rim, it has been speculated that the impact trajectory could have been from the southeastern direction (Miller, 2008, 2010).

Many impact craters are covered by postimpact sediments (e.g., Pilkington & Grieve, 1992), which makes surface study difficult (Koeberl, 1994). Geophysical studies can shed light on the thickness and architecture of the sedimentary cover or infill and the stratigraphy of the underlying impact crater. Many of those studies used gravimetry and magnetics (e.g., Brandt et al., 1998; Fudali, 1973; Ugalde et al., 2007), as well as seismics and ground-penetrating radar (e.g., Grant et al., 1997; Urbini et al., 2012). The electrical resistivity structure of impact craters has been studied by comparatively few authors using electrical current-based methods, such as electromagnetics (e.g., Adepelumi et al., 2005; Henkel, 1992; Masero & Fontes, 1991; Prado et al., 2019).

Previous geophysical studies at the Roter Kamm impact crater employed three different methods: gravity (Brandt et al., 1998; Fudali, 1973), magnetics (Brandt et al., 1998; Reimold et al., 1992), and ground-penetrating radar (Grant et al., 1997). The gravity data suggested a symmetric, bowl-shaped form of the Roter Kamm crater (Fudali, 1973). Gravimetric data modeling suggested a sedimentary thickness of about 300 m in the crater center (Brandt et al., 1998; Fudali, 1973). However, these studies assumed that the depth-to-diameter ratio is similar to the ones found at other simple impact structures (Fudali, 1973). Brandt et al. (1998) inferred a magnetic source body at a depth of 700–800 m, which matches the assumptions by Fudali (1973) regarding the base of the impact breccia above bedrock. The maximum negative gravity anomaly (−8.8 mGal) indicated strong brecciation of the material inside the crater (Brandt et al., 1998). Ground-penetrating radar measurements could only achieve a penetration depth of less than 5 m due to the moisture content originating from nightly fog leading to strong signal attenuation (Grant et al., 1997). Nevertheless, a calcrete crust was identified along the outer flank of the crater rim. This crust slopes toward the crater center with an angle of up to 22°, according to ground-penetrating radar data (Grant et al., 1997).

In contrast to the classical potential methods (magnetics and gravity) and the visual interpretation of ground-penetrating radar data previously used to study Roter Kamm, our transient electromagnetic (TEM) and audiomagnetotelluric (AMT) investigations can yield more reliable models of the subsurface. Using these methods, the sedimentary cover, the internal crater structure, and the crater infill can be imaged (e.g., Blanco-Arrué et al., 2022; Nienhaus et al., 2023; Yogeshwar & Tezkan, 2017). Another advantage of electromagnetic (EM) methods, such as TEM and AMT, is their sensitivity to the presence of fluids. The fluid content of a material greatly influences the bulk electrical conductivity (e.g., Archie, 1942). While the host material is resistive, even small amounts of water can lead to a significant decrease in resistivity. Besides water saturation, another important driver of conductivity can be clay content (Waxman & Smits, 1968; Winsauer & McCardell, 1953). Additionally, in crystalline bedrock, a decrease in resistivity has often been interpreted as an indication of increased fracturing (e.g., Henkel, 1992; Pilkington & Grieve, 1992).

Here, we present the first EM study of the Roter Kamm impact crater using TEM and AMT methods. Our results image the thickness and geometry of the postimpact sediment cover inside and outside of the impact crater and reveal the upper boundary of the breccia.

METHODS AND FIELD SURVEY

This section presents the methodology of our study. It includes a description of the geophysical methods, the survey design, and the data processing procedures.

The Transient Electromagnetic and Audiomagnetotelluric Methods

Electromagnetic methods are sensitive to electrical conductivity, the inverse of electrical resistivity, and are used to identify subsurface conductivity variations. High conductivities can be attributed to the presence of water as well as clay or ore minerals. Thus, EM methods are typically used for mineral exploration, groundwater detection, and imaging the stratigraphy of sedimentary basins (e.g., Blanco-Arrué et al., 2022; Danielsen et al., 2003; Mörbe et al., 2024; Zhang et al., 2025). We selected two EM methods to map the basement and sedimentary infill of the Roter Kamm impact crater: Transient electromagnetics (TEM) and Audiomagnetotellurics (AMT). The TEM method is especially capable of imaging shallow to intermediate depths (<500 m, Spies, 1989), whereas AMT can resolve resistivities up to a few kilometers depth (Simpson & Bahr, 2005). Combined, these methods can provide more reliable resistivity models over a wide depth range. Although both are based on the same physical principle of electromagnetic induction, they differ considerably in terms of resolution, application and data analysis.

The TEM method is an active EM method using a pulsed loop-source transmitter. For this study, we chose two different transmitter-receiver configurations: the single-loop and the fixed-loop geometry. The single-loop configuration uses one wire loop that serves simultaneously as transmitter and receiver, making this setup particularly time efficient and logistically beneficial, especially for small loop sizes. However, with increasing target depths, larger transmitter loops are required (Spies, 1989). Therefore, we additionally deployed a fixed-loop TEM configuration, where only one large transmitter loop is used with multiple independent receiver stations placed in and outside of the transmitter.

In contrast to the TEM method, AMT is a passive EM method, meaning that no artificial source is needed and naturally occurring EM field variations are used as source signal. The AMT method covers a frequency range from 1 to 10,000 Hz, allowing measurement of three magnetic field components and two horizontal electric components. The data are commonly presented as apparent resistivity and phase (termed as transfer functions). Both are derived from the ratio of the horizontal electric and magnetic field components. In the case of a two-dimensional subsurface, the derived transfer functions decouple in two modes, termed xy- and yx-polarization, where the electric field points in the x-direction and the magnetic field in the y-direction and vice versa. In case of a one-dimensional subsurface, both polarizations yield identical transfer functions.

Survey Design

The field survey focused on two perpendicular profiles transecting the Roter Kamm impact crater (Figure 1a,b). Profile P1 extends from southwest to northeast, whereas profile P2 is oriented from southeast to northwest. Profile P1 was densely sampled, including single-loop and fixed-loop TEM as well as AMT measurements, and is referred to as the main profile. It extends toward the Aurus Mountains in the northeast and perpendicular to the regional northwest-southeast fabric. Along profile P2, single-loop TEM measurements were conducted, using a single fixed-loop transmitter placed at the crater center. Along profile P1, we positioned four large fixed-loop transmitters with a size of 200 m $\times$ 200 m and a distance of 800 m between each transmitter center. Each source has 11 corresponding receiver stations along P1 with a maximum offset of 400 m from the center and a spacing between stations of 50 to 100 m. Inside the Roter Kamm crater, additional single-loop soundings with a smaller transmitter size of 100 m $\times$ 100 m were recorded to acquire shallow depth information.

We collected relatively sparse AMT data to complement the extensive TEM dataset and to acquire complementary information from greater depth. Eleven AMT soundings were recorded along P1 with a denser spacing inside the crater (Figure 1b). Due to a tight survey schedule and limited manpower, we omitted installing the vertical magnetic field sensors. Typically, two time series with sampling frequencies of 25,000 and 500 Hz were recorded at each sounding location for 10 and 20 min, respectively. Directly on the rim, as well as southwest of E2 and at the southwestern end of profile P1, the schedule settings of the logger unit were changed to optimize the time series recordings.

Along Profile P2, fixed-loop soundings were only carried out around the center of the impact crater, whereas the rest of the profile was only covered by single-loop soundings due to survey constraints (Figure 1b). One single-loop measurement was obtained on top of the northwestern crater rim using a 50 m × 50 m loop. All measurements along the regional profile were carried out using the small single-loop setup.

For the single-loop measurements the TEM-FAST 48 (AEMR, 2007), a lightweight and portable transmitter-receiver unit, was utilized. The equipment used for the fixed-loop measurement consists of the Zonge ZT-30 transmitter unit (Zonge, 2000) and two receiver units with induction coils: (1) SMARTem24 Geophysical Receiver System (ElectroMagnetic Imaging Technology [EMIT], 2018) plus Geonics 3-D-LF induction coils and (2) KMS-820 Data Acquisition Unit (KMS Technologies, 2019) plus two Zonge TEM/3 coils. The AMT data were collected with the SPAM Mk-IV system (Klose et al., 2011); the horizontal magnetic fields were recorded with the Metronix MFS07 broadband induction coils and the horizontal electric field with 60-m-long grounded dipoles.

Data Processing and Inversion Techniques

Transient Electromagnetic Method

Data processing included several steps, such as digital filtering, log-gating, and stacking. Firstly, the measured time series were digitally filtered using the three-point filter described by Mörbe (2020). This filter removes correlated noise generated by power lines ($f = 50$ Hz in Namibia), as well as possible time series amplitude shifts or linear drifts. A log-gating approach (Munkholm & Auken, 1996; Larsen et al., 2021) and, subsequently, a selective time gate-stacking scheme were used (Hanstein et al., 1986).

Comprehensive subsurface resistivity models were calculated along both profiles using a smoothness constrained Gauss-Newton based 3-D inversion algorithm (termed TEM3Dinv), enforcing smooth resistivity variations across the model (Blanco-Arrué, 2024; Liu et al., 2024). TEM3Dinv uses a staggered grid with hexahedral grid cells and assigned resistivity values for finite volume discretization (Yee, 1966). Topography has not been incorporated yet, which can pose a limitation when modeling data from rugged terrain. The data along the regional profile were interpreted using the well-established 1-D inversion algorithm EMU+ of the University of Cologne (e.g., Scholl, 2005; Yogeshwar, 2014). Due to the large interstation distance along the regional profile, a 3-D interpretation was not feasible. A combined inversion of TEM and AMT data was carried out for one sounding at the center of the Roter Kamm crater, as the data indicated a one-dimensional electrical resistivity distribution. For this purpose, we applied the Marquardt–Levenberg scheme, which employs a reduced number of predefined layers with sharp interfaces (Levenberg, 1944; Marquardt, 1963).

As a measure of data fitting, the error-weighted root-mean-square (wRMS) was calculated:

$$\mathrm{wRMS} = \sqrt{\frac{1}{N}\sum_{i=1}^{N}\left(\frac{d_{\mathrm{obs}} - d_{\mathrm{calc}}}{\Delta d_{\mathrm{obs}}}\right)^2} \tag{1}$$

with N being the number of data, d_{obs} and d_{calc} the observed and calculated data and Δd_{obs} the corresponding data error. A wRMS-value of 1 indicates that the model explains the data optimally.

To evaluate the reliability of the model in terms of depth of investigation (DOI), we used two different formulations. For the 3-D model, the DOI estimate was based on the model sensitivity, which takes into account the source-receiver geometry, data information content, and data error, as well as the modeled conductivity distribution (Christiansen & Auken, 2012). For one-dimensional DOI estimations, the Spies formula was used (Spies, 1989). It considers the transmitter moment, the average electrical resistivity, and the noise level, but discards the source-receiver geometry. Depending on the subsurface conductivity and the transmitter-receiver configuration, different depth ranges can be targeted.

Audiomagnetotelluric Method

To estimate the transfer functions, the AMT data were processed following Ritter et al. (1998). We used the MARE2DEM algorithm to derive a 2-D subsurface resistivity model (Key, 2016). While finite difference discretization is incorporated for the 3-D TEM inversion algorithm, MARE2DEM uses finite elements on a triangular mesh. The algorithm can include topography along the profile line.

Before applying MARE2DEM, the dimensionality of the data was analyzed to ensure it is not predominantly influenced by 3-D effects and distorted by off profile resistivity variations. We used a skewness criterion to verify approximate two-dimensionality conditions for the Roter Kamm target, and in addition analyzed the strike angle of each sounding (Bahr, 1988). The geological strike direction aligns with the orientation of geological features such as fault zones and is ideally perpendicular to the profile layout.

RESULTS

First, we present representative TEM and AMT data examples, and analyze their dimensionality to assess the nature and complexity of the subsurface. Subsequently, we introduce the derived resistivity models, providing insights to the spatial distribution of subsurface resistivities and their potential geological causes.

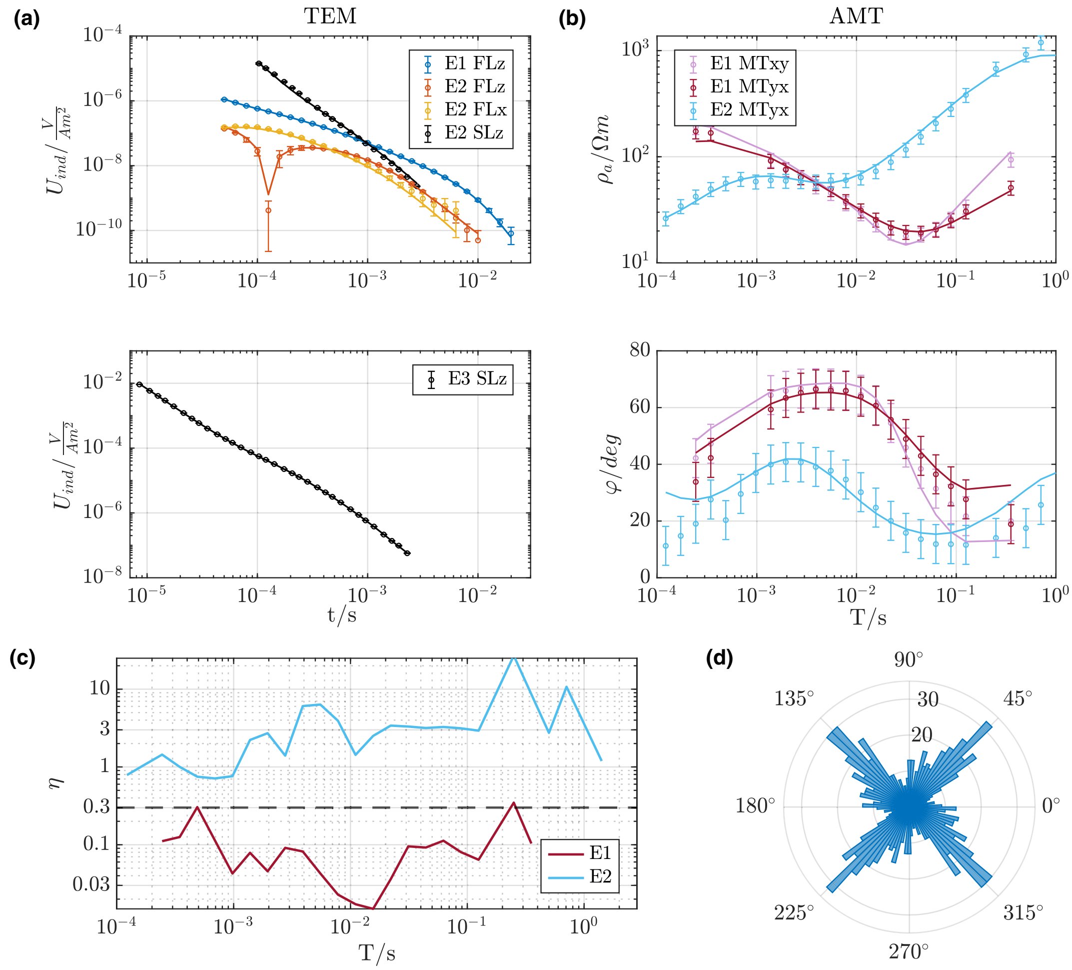

FIGURE 3. Transient electromagnetic (TEM) and audiomagnetotelluric (AMT) data examples and AMT dimensionality analysis along profile P1, with E1 at the center of the crater, E2 at the crater rim, and E3 halfway between the Roter Kamm crater and the Aurus Mountains (cf. locations in Figure 1a,b). The measured data and error (circle with error bar), as well as the modeled data from the inversions (1-D/3-D TEM and 2-D AMT) are depicted by a line. (a) Voltage decay versus transient time for fixed-loop soundings (FL, upper panel) and a single-loop measurement (SL) with a transmitter size of 50 × 50 m^2 (lower panel). (b) AMT transfer functions, apparent resistivity (upper panel) and phase (lower panel). No usable transfer functions of the xy-polarization data exist at location E2. (c) Skewness η for the sounding E1 at the center of the crater and E2 located on top of the crater rim (E2). (d) Rose diagram for all AMT stations with 0° indicating magnetic North. (Color figure can be viewed at wileyonlinelibrary.com)

Data Examples and Dimensionality Analysis

Figure 3 shows three data examples from sounding locations E1, E2, and E3 in Figure 1a,b. The single-loop sounding data along the regional profile (E3 SLz, transmitter size 50 × 50 m^2) cover early times starting at 8 µs up to 2.3 ms, providing shallow depth information. The change in temporal decay characteristics indicates the presence of a conductive layer below a resistive overburden. The fixed-loop data (for locations E1 and E2) span a time range from 50 µs to 20 ms. Sounding E2 is an example from the crater rim with a 400 m offset between transmitter and receiver. The transmitter-receiver geometry causes the sign reversal in the vertical component (E2 FLz) at $t \approx 1.5 \times 10^{-4}$ s. Both measured x- and z-components (E2 FLx and FLz) show a comparable decay rate at later times. The transient at the center of Roter Kamm (E1 FLz) was measured in the center of the transmitter loop and, therefore, has a higher voltage amplitude. The strong decay at later times indicates a deep resistive base layer. As the Roter Kamm crater presents a multidimensional target, a reliable analysis of the data requires sophisticated TEM inversion schemes.

The AMT apparent resistivity and phase curves from the center of the impact crater (E1 MT) and its rim (E2 MT) are presented in Figure 3b. Note that for the xy-polarization no reliable transfer functions were obtained at sounding location E2 (cf. Figure 1b for location). The curves clearly show different subsurface characteristics between locations E1 and E2. Whereas the apparent resistivity at the crater rim indicates an increase of resistivity with depth, the data from the center of the crater suggest a three-layered case with a conductive layer between two resistors. The apparent resistivity behavior is confirmed by the period dependency of the observed phase values.

The agreement of both polarizations at sounding location E1 at the crater center suggests a 1-D subsurface distribution. This is in accordance with the frequency behavior of the skewness η in Figure 3c, which is mostly below the threshold value of 0.3, indicating the absence of any 3-D data distortion effects (Bahr, 1991). The data measured on top of the rim are the only exception with significantly higher skewness values over the entire frequency range (Figure 3c). This is a clear indication of a multidimensional subsurface. However, we observe a consistent pattern of all calculated strike angles for all AMT soundings shown in the rose diagram (Figure 3d). Based on the general faulting in the area (Thomas et al., 2016), and the profile angle transecting the crater rim, 46° N appears to be a reasonable strike direction.

The Resistivity Models

To derive a minimum layered model with sharp boundaries for the center of the Roter Kamm crater, we applied a 1-D joint Marquardt–Levenberg inversion (Marquardt, 1963) of the AMT (*xy*-polarization) and TEM data. The model shows a four-layered depth profile down to 600 m depth (Figure 4a).

The shallow 80 Ωm surface layer with a thickness of 25 m (Layer 1) is followed by a 1000 Ωm layer (thickness: 85 m, Layer 2), a 10 Ωm conductor (thickness: 230 m, Layer 3), and a 1000 Ωm resistive base layer (Layer 4). The narrow range of equivalent models, which fit the data well, indicates that the upper boundary and resistivity of Layer 3 are resolved well. The lower boundary is imaged at 340 m depth with an accuracy of ±30 m, and the DOI estimates to 630 m for TEM and 9500 m for AMT. Both DOIs clearly exceed the lower interface. The resistivities of Layers 2 and 4 are not resolved well, as TEM and AMT are most sensitive to conductors. Layer 1 is also not well resolved, because, besides the high resistivity, the frequency and time ranges of the AMT and TEM data do not provide sufficient shallow depth information.

All multidimensional inversions were carried out using a 100 Ωm homogeneous starting model. The 3-D TEM inversion includes the two components of the fixed-loop data and the additional single-loop data, whereas the 2-D AMT inversion includes both polarizations, except on the crater rim, where only the *xy*-polarization data were used due to strong 3-D data distortion. The two-dimensional resistivity sections along both profiles reveal a conductive anomaly shaped like a convex lens embedded in a resistive surrounding (Figure 4b,c). The lens is located exactly between the crater rims at a depth of 80 m below the surface. Both methods resolve the boundaries of the conductor along P1 equally well and are in good agreement. Although a smoothness-constrained inversion technique was used, the comparison of the resistivity-depth profiles extracted from the 2-D AMT and 3-D TEM models at the center of the crater compares well against the 1-D AMT + TEM joint inversion result, validating the results of both methods (Figure 4a).

The shape of the anomaly is not fully symmetric, as the slope of the lower boundary is steeper at the northwestern part of P2 and the northeastern part of P1. However, whereas the TEM models resolve the horizontal extent of the conductor better due to the increased data coverage, the AMT method has an improved depth resolution. Due to the low-frequency AMT data, the structure underneath the conductive lens is resolved better. The resistivity underneath the conductive lens appears to increase with depth to high values exceeding 1000 Ωm. The lens extends horizontally approximately 1450 m in northeast–southwest direction and 1900 m in northwest–southeast direction, indicating a slight asymmetry of the crater interior. Inside the crater, the sensitivity-based DOI indicates the lower boundary of the conductive anomaly rather than the lower resolution limit. Therefore, the two definitions of the DOI indicate different resolution depths. Below the crater rim, no other conductive anomalies are detected.

Outside of the impact structure, a conductive layer is imaged along the regional profile (cf. Figure 1a), which extends from the rim at a depth of around 50 m toward the northeast (Figure 4d). This layer has a similar resistivity as the conductive lens. It continues toward the Aurus Mountains with increasing thickness and slightly increasing resistivity.

DISCUSSION

The derived conductivity models can shed light on the shape and the nature of the infill of the Roter Kamm impact crater. The AMT and TEM results reveal the geometry, thickness, and internal structure of the sedimentary infill, which can provide information concerning postimpact deposition in dependence on regional climatic and environmental histories.

Postimpact Sediments

We distinguished three layers with different electrical properties in the central part of the impact crater, possibly all representing sedimentary infill (Figure 4).

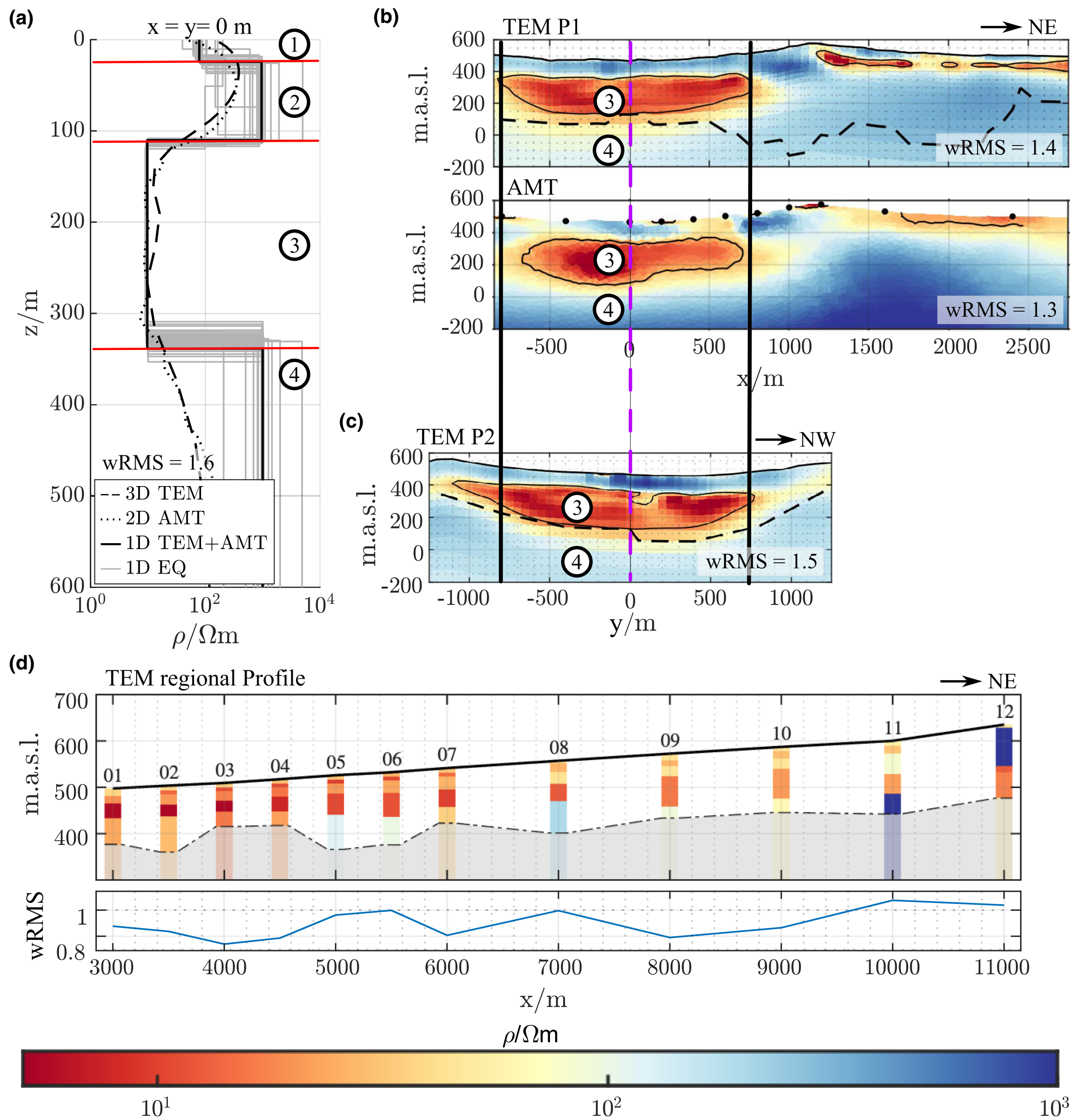

FIGURE 4. Inversion models for transient electromagnetic (TEM) and audiomagnetotelluric (AMT) data. Numbers mark the common features in the different models. (a) 1-D model of AMT and TEM data compared with the resistivity-depth profiles extracted from the 3-D TEM and 2-D AMT models. Layer boundaries are highlighted in red. The depth of investigation (DOI) for the 1-D AMT model is 9500 m, while it is 630 m for the 1-D TEM model. (b) 3-D TEM model along profile P1 (upper panel) and 2-D AMT model along P1 (lower panel). Whereas the AMT stations are marked in black. The DOI for the AMT model is outside of the presented axes. (c) 3-D TEM model along profile P2 with the DOI indicated as a black line. The horizontal dimension of the conductive lens is indicated by continuous black lines, and the center of the Roter Kamm impact crater by a dashed purple line. (d) 1-D Marquardt–Levenberg inversions of all TEM soundings along the regional profile. The DOI is marked by a black dashed line. Topography data taken from National Aeronautics and Space Administration Jet Propulsion Laboratory [NASA JPL] (2022). (Color figure can be viewed at wileyonlinelibrary.com)

Layer 3 is of planoconvex shape and the most prominent feature. The resistivity variations within the sediments may be attributed to different moisture contents, as the presence of ore minerals is unlikely inside an impact crater, where the target rock did not contain such minerals prior to impact. Following Archie's law for clay-free sediments, the higher the moisture content, the higher the conductivity (Archie, 1942). Hence, the conductive lens probably marks a zone of particularly high moisture content or accumulation of water, whereas the upper two layers are comparatively dry. As the topmost layer (Layer 1) is slightly more conductive than

Layer 2, it may contain a relatively higher moisture content, likely resulting from nightly fog. This interpretation is supported by zones of increased vegetation observed across the crater surface during the field survey in March 2022.

Archie (1942) described an empirical relation connecting the resistivity of a pore fluid with bulk resistivity. Archie's law is based on several rock parameters, such as saturation and pore geometry. Dickinson and Ward (1994) measured an average porosity of 34% for eolian sediments in the Namib desert. To estimate the fluid conductivity using Archie's law, we assumed fully saturated, unconsolidated sand within the conductive lens with a tortuosity factor of 0.88 and a cementation exponent of 1.37 (Keller, 1988). Using the modeled bulk resistivity ($\rho_b \approx 10\ \Omega$m), we estimated fluid resistivity of $\rho_{fl} = \rho_b/F \approx 2.6\ \Omega$m. Interestingly, a water sample we collected during the field survey from a borehole in the Aurus Mountains (−27.588266° N, 16.399952° E) approximately 23 km to the northeast of Roter Kamm has a resistivity of 1.85 Ωm at a temperature of 20.1°C. Whereas the fluids occurring at Roter Kamm and at the borehole might not have the same origin, it shows that highly conductive fluids are present in the vicinity of the survey area. However, an accurate analysis of water saturation and pore-fluid resistivity would only be possible if the rock formation parameters were known, for example from borehole data.

The similar resistivities of the conductive lens and the layer outside of the crater suggest that the material composition is comparable. The layer outside the crater extends more than 10 km toward the Aurus Mountains and therefore cannot be attributed to ejecta from the crater. The conductivities of the investigated structures are considerably lower than those modeled at the Aurus clay pan (Nienhaus et al., 2023), northwest of Roter Kamm (Figure 1a). This suggests that the conductive structures are unlikely to contain a particularly high clay content. Thus, the presence of eolian sediments covering the entire area, as suggested by Miller (2010) and Grant et al. (1997), appears most likely.

Boundary Between Breccia and Postimpact Sediments

As no deep borehole information is available, the geophysical models cannot be uniquely calibrated with ground-truth data. The resistivity boundary between Layers 3 and 4 in Figure 3 occurs at a depth of 340 ± 30 m in the central crater. This interface can be interpreted in three different ways, depending primarily on the assumed permeability and water saturation. In all three cases, we assume that no metallogenetic minerals (such as pyrite or magnetite), which could account for the observed high-conductivity anomalies, are present within the impact crater. This is supported by previous rock chemical analyses (cf. Reimold et al., 1994; Reimold & Miller, 1989). The upper two layers are most likely composed of eolian sediments, whereas the composition of the deeper layers is less constrained, giving rise to three alternative scenarios.

Scenario A

The boundary to Layer 4 at 340 m depth represents the top of the fractured bedrock, which acts as a hydraulic barrier. In this scenario, the Roter Kamm impact crater would be significantly shallower than other craters of comparable diameter (Grieve, 1987; Pike, 1980). Empirical relationships for the altitude difference between the crater rim and the top of the breccia layer, and between the rim and the top of the bedrock depth, predict significantly greater bedrock depth for Roter Kamm crater (Grieve, 1987; Pike, 1980), namely: 360 m for rim to breccia and 680 m for rim to bedrock.

Considering an elevation of the crater rim of 130 m higher than the surface at the center of the impact crater, the maximum altitude difference between the rim top and the top of Layer 4 in the crater center is estimated to be 470 ± 30 m. This estimate is closer to the estimated rim-to-breccia altitude difference at the top of Layer 4. Furthermore, scenario A is contradictory to the previous findings of Fudali (1973) and Brandt et al. (1998) in terms of the depth estimations for the sediments and brecciated material. Therefore, we regard scenario A as unlikely.

Scenario B

The boundary to Layer 4 at 340 m depth reflects the top of the breccia, which is assumed to be sealed against water from the postimpact sediments by a barrier of clay. This scenario aligns more closely with previous geophysical findings and the general understanding of simple impact craters. However, the formation of such a clay layer would require a stagnant water body for many years that is fed by fluvial supply and associated transport of material. This is unlikely, taking into account the fact that the Namib Desert has existed continuously since Middle Miocene times (Senut & Ségalen, 2014), prior to the formation of the Roter Kamm crater circa 4–5 million years ago (Hecht et al., 2008; Koeberl et al., 1993). Moreover, Miller (2008, 2010) did not find any signs of fluvial activity after crater formation. Another argument against the existence of a clay layer above the breccia comes from geophysical and geological investigations of the Aurus Clay Pan by Nienhaus et al. (2023), which is located around 10 km northwest of the Roter Kamm crater (see Figure 1a). The sediments in this clay pan consist of clays to sands that are fluvially supplied from a large catchment by irregular rain events. Their electrical resistivities ($\rho = 4.6\ \Omega$m) are much lower than those found inside the Roter Kamm crater. Hence, scenario B is also regarded as unlikely.

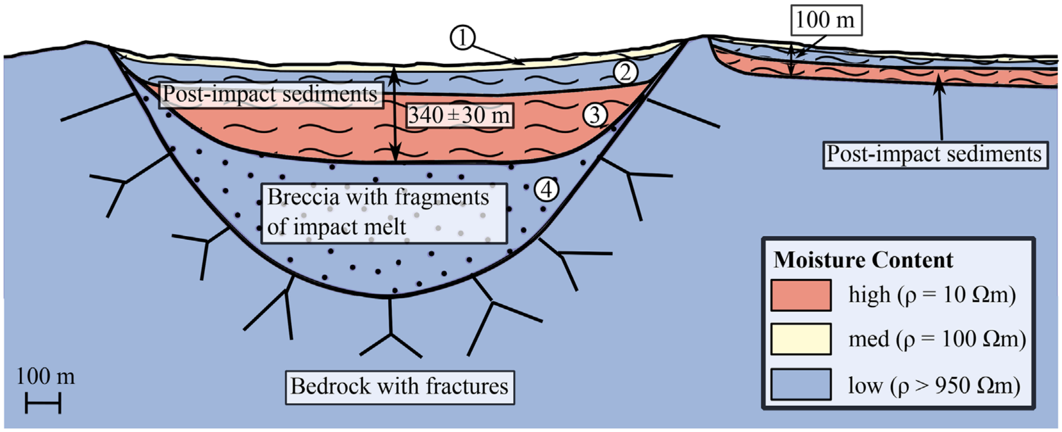

FIGURE 5. Schematic representation of the Roter Kamm impact crater along profile P1 (modified after Fudali, 1973; Reimold & Miller, 1989). (Color figure can be viewed at wileyonlinelibrary.com)

Scenario C

The boundary to Layer 4 at 340 m depth reflects the top of the breccia, which is assumed to be sealed against water from the postimpact sediments by a barrier of cemented calcrete. This hypothesis also requires water to have been present at an early stage after the formation of the Roter Kamm impact crater. However, the amount of water would be much less than for scenario B, as a cemented calcrete crust does not require a stagnant water body but can be formed by irregular rain events and precipitation of calcite from temporary ponds and pore water. This model is further supported by the finding of a calcrete crust outside the impact crater (Grant et al., 1997), although it cannot explain why calcretization was concentrated at the boundary between the breccia and the postimpact sediments. Based on these arguments, we consider scenario C to be the most likely one.

Consequently, we expanded the conceptual model presented in Fudali (1973) and Reimold and Miller (1989) to include the interpretation of the resistivity models gained from the EM measurements. As a result, the volume of the postimpact sediments in the Roter Kamm crater can be estimated to approximately 0.34 km^3. The value of 340 ± 30 m for their maximum thickness is in the same size range as discussed in previous studies (e.g., Brandt et al., 1998; Fudali, 1973). The asymmetry along the profile in the southeast–northwest direction could indicate a northwesterly impact direction (Elbeshausen & Wünnemann, 2011), which agrees well with the assumed impact direction by Miller (2010). Based on observations during previous field studies, the rim of the impact crater is not covered by any sediments (Dietz, 1965; Fudali, 1973; Reimold & Miller, 1989), which explains the absence of any conductive anomaly at the crater rim.

Shape of the Roter Kamm Impact Crater

Previous resistivity studies of other impact craters showed lower resistivities of breccia compared with the fractured bedrock (Adepelumi et al., 2005; Henkel, 1992; Unsworth et al., 2002). However, the EM data presented here do not provide any direct information on the breccia-to-bedrock boundary. Even the AMT data, which provide resolution for greater depths, do not resolve any deeper resistivity interfaces that indicate bedrock. This is probably due to the presence of the large conductive anomaly inside Roter Kamm, which reduces the sensitivity of the AMT method to any underlying structures. Figure 5 shows a sketch (modified after Fudali, 1973, and Reimold & Miller, 1989) combined with the derived electrical resistivity values, identified subsurface interfaces, and the assumed moisture contents. The bedrock surface, as illustrated in Figure 5, and thus the crater shape, are based on the study presented in Fudali (1973) and not on the EM data presented here.

CONCLUSIONS

We present the first electrical resistivity models of the Roter Kamm impact crater, imaging the extensive sediment cover and revealing the surface of the impact breccia above bedrock. Our geophysical model proves the simple structure of the impact crater. The remarkable agreement between both applied electromagnetic methods validates the quality of our data and the reliability of our results. The breccias of the Roter Kamm crater are comparatively resistive and indistinguishable from the bedrock, suggesting that conductive anomalies primarily reflect postimpact sedimentation and subsequent hydrogeological processes. These results highlight the potential of EM methods as a supplementary approach to gravimetric and magnetic studies in impact crater research. The thickness of the postimpact sediments reaches a maximum depth of 340 ± 30 m around the approximate center of the crater. However, both profiles show a slight asymmetry in the breccia surface, which is tentatively considered to support a northwesterly impact direction, as also referred to in earlier studies. The resistivity structure inside the sedimentary fill indicates three different layers. Based on their resistivities, it is likely that Roter Kamm captured considerable water in the past 4–5 million years. Our results provide information concerning the thickness and layering of the sediments in the Roter Kamm crater. However, only scientific drilling can answer details on sediment composition and, thus, paleoclimatic conditions that have controlled the environmental setting and the types of sediments deposited.

Acknowledgments—This project was funded by the Deutsche Forschungsgemeinschaft (DFG, project number: 268236062) as part of the Collaborative Research Center (CRC) 1211. We thank the Bundesanstalt für Geowissenschaften und Rohstoffe (BGR) for providing the TEM-FAST 48 and the Geophysical Instrument Pool Potsdam (GIPP) for providing the AMT equipment (grant: 202127). We are also grateful to the colleagues from the University of Namibia, and all other participants in the field campaign in February/March 2022 for their competent help in retrieving the geophysical data. The authors would like to express their gratitude toward the Museum für Naturkunde—Leibniz-Institut für Evolutions- und Biodiversitätsforschung for fruitful and interesting discussions about impact craters. We also thank Jüri Plado, an anonymous reviewer, and the editor Wolf Uwe Reimold for their valuable comments and suggestions that helped improve this manuscript. We are happy to support the special issue of Meteoritics and Planetary Science dedicated to the work of Christian Koeberl, who worked extensively on the Roter Kamm impact crater. Open Access funding enabled and organized by Projekt DEAL.

Data Availability Statement—The data that support the findings of this study are openly available in Zenodo at https://doi.org/10.5281/zenodo.17193374.

Editorial Handling—Dr. A. J. Timothy Jull

REFERENCES

Adepelumi, A., Fontes, S. L., Schnegg, P. A., and Flexor, J. 2005. An Integrated Magnetotelluric and Aeromagnetic Investigation of the Serra da Cangalha Impact Crater, Brazil. *Physics of the Earth and Planetary Interiors* 150: 159–181. https://doi.org/10.1016/j.pepi.2004.08.029.

Applied Electromagnetic Research – AEMR. 2007. *TEM-FAST 48 HPC (Manual v.8a)*. http://www.aemr.net/.

Archie, G. 1942. The Electrical Resistivity Log as an Aid in Determining some Reservoir Characteristics. *Transactions of American Institute of Mining Metallurgical Engineers* 146: 54–62. https://doi.org/10.2118/942054-G.

Bahr, K. 1988. Interpretation of the Magnetotelluric Impedance Tensor: Regional Induction and Local Telluric Distortion. *Journal of Geophysics* 62: 119–127. https://journal.geophysicsjournal.com/jofg/article/view/129.

Bahr, K. 1991. Geological Noise in Magnetotelluric Data: A Classification of Distortion Types. *Physics of the Earth and Planetary Interiors* 66: 24–38. https://doi.org/10.1016/0031-9201(91)90101-M.

Blanco-Arrué, B. 2024. "Multidimensional transient electromagnetic data for the exploration of clay pans in the Atacama Desert, Chile." PhD thesis, University of Cologne. http://kups.ub.uni-koeln.de/id/eprint/72721.

Blanco-Arrué, B., Yogeshwar, P., Tezkan, B., Mörbe, W., Díaz, D., Farah, B., Buske, S., et al. 2022. Exploration of Sedimentary Deposits in the Atacama Desert, Chile, Using Integrated Geophysical Techniques. *Journal of South American Earth Sciences* 115: 103746. https://doi.org/10.1016/j.jsames.2022.103746.

Brandt, D., Reimold, W. U., Franzsen, A. J., Koeberl, C., and Wendorff, L. 1998. Geophysical Profile of the Roter Kamm Impact Crater, Namibia. *Meteoritics & Planetary Science* 33: 447–453. https://doi.org/10.1111/j.1945-5100.1998.tb01649.x.

Christiansen, A. V., and Auken, E. 2012. A Global Measure for Depth of Investigation. *Geophysics* 77: WB171–WB177. https://doi.org/10.1190/geo2011-0393.1.

Collins, G. S., Melosh, H. J., and Osinski, G. R. 2012. The Impact-Cratering Process. *Elements* 8: 25–30. https://doi.org/10.2113/gselements.8.1.25.

Danielsen, J., Auken, E., Jørgensen, F., Søndergaard, V., and Sørensen, K. I. 2003. The Application of the Transient Electromagnetic Method in Hydrogeophysical Surveys. *Journal of Applied Geophysics* 53: 181–198. https://doi.org/10.1016/j.jappgeo.2003.08.004.

Dence, M. R. 1972. The Nature and Significance of Terrestrial Impact Structures. In *Proceedings of the 24th International Geological Congress*, edited by J. E. Gill, A. M. Goodwin, and H. R. Wynne-Edwards, 77–89. Montreal: 24th International Geological Congress.

Dickinson, W. W., and Ward, J. D. 1994. Low Depositional Porosity in Eolian Sands and Sandstones, Namib Desert. *Journal of Sedimentary Research* 64(2a): 226–232. https://doi.org/10.1306/D4267D66-2B26-11D7-8648000102C1865D.

Dietz, R. S. 1965. Roter Kamm, Southwest Africa: Probable Meteorite Crater. *Meteoritics* 2: 311–14. https://doi.org/10.1111/j.1945-5100.1965.tb01438.x.

Elbeshausen, D., and Wünnemann, K. 2011. "The Effect of Target Topography and Impact Angle on Crater Formation—Insight from 3D Numerical Modelling." *42nd Lunar and Planetary Science Conference*. p. 1778.

ElectroMagnetic Imaging Technology. 2018. *USER GUIDE for the SMARTem24 and DigiAtlantis Systems*.

Environmental Systems Research Institute. 2022. *World Imagery*. Accessed March 13, 2023. https://server.arcgisonline.com/ArcGIS/rest/services/World_Imagery/MapServer/tile/{z}/{y}/{x}.

French, B. M., and Koeberl, C. 2010. The Convincing Identification of Terrestrial Meteorite Impact Structures: What Works, What doesn't, and why. *Earth-Science Reviews* 98: 123–170. https://doi.org/10.1016/j.earscirev.2009.10.009.

Fudali, R. F. 1973. Roter Kamm: Evidence for an Impact Origin. *Meteoritics* 8: 245–257. https://doi.org/10.1111/j.1945-5100.1973.tb01253.x.

Gottwald, M., Kenkmann, T., and Reimold, W. U. 2020. *Terrestrial Impact Structures: The TanDEM-X Atlas*. Munich: Verlag Dr. Friedrich Pfeil.

Grant, J. A., Koeberl, C., Reimold, W. U., and Schultz, P. H. 1997. Gradation of the Roter Kamm Impact Crater, Namibia. *Journal of Geophysical Research: Planets* 102 (E7): 16327–38. https://doi.org/10.1029/97JE01315.

Grieve, R. A. 1987. Terrestrial impact structures. *Annual Review of Earth and Planetary Sciences* 15: 245–270. https://doi.org/10.1146/annurev.earth.15.1.245.

Hanstein, T., Eilenz, H., and Strack, K. 1986. Einige Aspekte der Aufbereitung von LOTEM Daten. In *Protokoll über das 11. Kolloquium für Elektromagnetische Tiefenforschung*, edited by V. Haak, and J. Homilius. Potsdam: Deutsche Geophysikalische Gesellschaft. https://gfzpublic.gfz-potsdam.de/rest/items/item_5013724_2/component/file_5013725/content.

Hecht, L., Reimold, W. U., Sherlock, S., Tagle, R., Koeberl, C., and Schmitt, R. 2008. New Impact-Melt Rock from the Roter Kamm Impact Structure, Namibia: Further Constraints on Impact Age, Melt Rock Chemistry, and Projectile Composition. *Meteoritics and Planetary Science* 43: 1201–18. https://doi.org/10.1111/j.1945-5100.2008.tb01123.x.

Henkel, H. 1992. Geophysical Aspects of Meteorite Impact Craters in Eroded Shield Environment, with Special Emphasis on Electric Resistivity. *Tectonophysics* 216: 63–89. https://doi.org/10.1016/0040-1951(92)90156-Z.

Keller, G. V. 1988. Rock and Mineral Properties. In *Investigations in Geophysics: Vol. 3. Electromagnetic Methods in Applied Geophysics: Volume 1, Theory*, edited by M. N. Nabighian, 13–48. Oklahoma: Society of Exploration Geophysicists.

Kenkmann, T. 2021. The Terrestrial Impact Crater Record: A Statistical Analysis of Morphologies, Structures, Ages, Lithologies, and More. *Meteoritics and Planetary Science* 56: 1024–70. https://doi.org/10.1111/maps.13657.

Key, K. 2016. MARE2DEM: A 2-D Inversion Code for Controlled-Source Electromagnetic and Magnetotelluric Data. *Geophysical Journal International* 207: 571–588. https://doi.org/10.1093/gji/ggw290.

Klose, R., Schmidt, G., Ritter, O., and Dawes, G. 2011. What Is SPAM Four for? In *Protokoll über das 24. Schmucker-Weidelt-Kolloquium für Elektromagnetische Tiefenforschung: Neustadt an der Weinstraße 19.-23. September 2011*, edited by R. Börner, and K. Schwalenberg, 127–134. Potsdam: Deutsche Geophysikalische Gesellschaft. https://gfzpublic.gfz-potsdam.de/rest/items/item_65327_1/component/file_65325/content.

KMS Technologies. 2019. *KMS-820 Data Acquisition Unit*. https://kmstechnologies.com/KMS_820.html.

Koeberl, C. 1994. African Meteorite Impact Craters: Characteristics and Geological Importance. *Journal of African Earth Sciences* 18: 263–295. https://doi.org/10.1016/0899-5362(94)90068-X.

Koeberl, C., Hartung, J. B., Kunk, M. J., Klein, J., Matsuda, J.-I., Nagao, K., Reimold, W. U., and Storzer, D. 1993. The Age of the Roter Kamm Impact Crater, Namibia: Constraints from ^{40}Ar-^{39}Ar, K-Ar, Rb-Sr, Fission Track, and ^{10}Be-^{26}Al Studies. *Meteoritics* 28: 204–212. https://doi.org/10.1111/j.1945-5100.1993.tb00758.x.

Larsen, J. J., Pedersen, S. S., Foged, N., and Auken, E. 2021. Suppression of Very Low Frequency Radio Noise in Transient Electromagnetic Data with Semi-Tapered Gates. *Geoscientific Instrumentation, Methods and Data Systems* 10: 81–90. https://doi.org/10.5194/gi-10-81-2021.

Levenberg, K. 1944. A Method for the Solution of Certain Non-linear Problems in Least Squares. *Quarterly of Applied Mathematics* 2: 164–68. https://doi.org/10.1090/qam/10666.

Liu, Y., Yogeshwar, P., Peng, R., Hu, X., Han, B., and Blanco-Arrué, B. 2024. Three-Dimensional Inversion of Time-Domain Electromagnetic Data Using Various Loop Source Configurations. *IEEE Transactions on Geoscience and Remote Sensing* 62: 1–15. https://doi.org/10.1109/TGRS.2024.3383288.

Marquardt, D. W. 1963. An Algorithm for Least-Squares Estimation of Nonlinear Parameters. *Journal of the Society for Industrial and Applied Mathematics* 11: 431–441. http://www.jstor.org/stable/2098941.

Masero, W. C. B., and Fontes, S. L. 1991. Audiomagnetotelluric Investigation of the Colonia Depression, São Paulo – Brazil. In *2nd International Congress of the Brazilian Geophysical Society*. Bahia: European Association of Geoscientists and Engineers. https://doi.org/10.3997/2214-4609-pdb.316.61.

Miller, R. 2008. Meteorite Impact Craters and Meteorites. In *The Geology of Namibia*, edited by R. Miller, 26-1–26-18. Windhoek: Ministry of Mines and Energy.

Miller, R. 2010. Roter Kamm Impact Crater of Namibia: New Data on Rim Structure, Target Rock Geochemistry, Ejecta, and Meteorite Trajectory. In *Special Paper/The Geological Society of America: 465. Large Meteorite Impacts and Planetary Evolution IV*, edited by R. L. Gibson, and W. U. Reimold. Boulder, CO: Geological Society of America. https://doi.org/10.1130/2010.2465(24).

Mörbe, W. 2020. "Deep Controlled Source Electromagnetics for Mineral Exploration: A Multidimensional Validation Study in Time and Frequency Domain." PhD thesis, University of Cologne. http://kups.ub.uni-koeln.de/id/eprint/10696.

Mörbe, W., Yogeshwar, P., Tezkan, B., Kotowski, P., Thiede, A., Steuer, A., Rochlitz, R., Günther, T., Brauch, K., and Becken, M. 2024. Large-Scale 3D Inversion of Semi-Airborne Electromagnetic Data—Topography and Induced Polarization Effects in a Graphite Exploration Scenario. *Geophysics* 89: B339–B352. https://doi.org/10.1190/geo2023-0471.1.

Munkholm, M. S., and Auken, E. 1996. Electromagnetic Noise Contamination on Transient Electromagnetic Soundings in Culturally Disturbed Environments. *Journal of Environmental and Engineering Geophysics* 1: 119–127. https://doi.org/10.4133/JEEG1.2.119.

National Aeronautics and Space Administration Jet Propulsion Laboratory. 2022. *NASADEM Merged DEM Global 1 Arc Second V001 [Data Set]*. Pasadena, CA: NASA EOSDIS Land Processes DAAC. Accessed March 13, 2023. https://doi.org/10.5067/MEaSUREs/NASADEM/NASADEM_HGT.001.

Nienhaus, H., Yogeshwar, P., Mörbe, W., Tezkan, B., Büttner, C., Legler, M., Buske, S., Lushetile, B., Wennrich, V., and Melles, M. 2023. Geophysical and Geological Exploration of the Aurus Clay Pan as an Archive of the Long-Term Climatic and Environmental History of the Namib Desert. *Global and Planetary Change* 230: 104259. https://doi.org/10.1016/j.gloplacha.2023.104259.
Osinski, G. R., Grieve, R. A. F., Ferrière, L., Losiak, A., Pickersgill, A. E., Cavosie, A. J., Hibbard, S. M., et al. 2022. Impact Earth: A Review of the Terrestrial Impact Record. *Earth-Science Reviews* 232: 104112. https://doi.org/10.1016/j.earscirev.2022.104112.
Osinski, G. R., and Pierazzo, E. 2013. Impact Cratering: Processes and Products. In *Impact Cratering: Processes and Products*, edited by G. R. Osinski and E. Pierazzo, 1–20. Chichester, UK: Wiley-Blackwell. https://doi.org/10.1002/9781118447307.
Pike, R. J. 1980. Formation of Complex Impact Craters: Evidence from Mars and Other Planets. *Icarus* 43: 1–19. https://doi.org/10.1016/0019-1035(80)90083-4.
Pilkington, M., and Grieve, R. A. 1992. The Geophysical Signature of Terrestrial Impact Craters. *Reviews of Geophysics* 30: 161–181. https://doi.org/10.1029/92RG00192.
Prado, R. L., Espin Fenoll, I. C., Ullah, I., Miura, G. C. M., Crósta, A. P., Zanon dos Santos, R. P., Reimold, W. U., et al. 2019. Geophysical Investigation of the Colônia Structure, Brazil. *Meteoritics and Planetary Science* 54: 2357–72. https://doi.org/10.1111/maps.13292.
Reimold, W. U., Koeberl, C., and Bishop, J. 1994. Roter Kamm Impact Crater, Namibia: Geochemistry of Basement Rocks and Breccias. *Geochimica et Cosmochimica Acta* 58: 2689–2710. https://doi.org/10.1016/0016-7037(94)90138-4.
Reimold, W. U., and Miller, R. 1989. "The Roter Kamm Impact Crater, SWA/Namibia." *Proceedings of the Lunar and Planetary Science Conference*. pp. 711–732.
Reimold, W. U., Reid, A. M., Jakes, P., Zolensky, M., and Miller, R. 1992. A Magnetic Survey across the Roter Kamm Impact Crater, Namibia. In *Abstracts of the Lunar and Planetary Science Conference*, vol. 23, 1143. Houston, TX: Lunar and Planetary Institute.
Ritter, O., Junge, A., and Dawes, G. J. 1998. New Equipment and Processing for Magnetotelluric Remote Reference Observations. *Geophysical Journal International* 132: 535–548. https://doi.org/10.1046/j.1365-246X.1998.00440.x.
Schmieder, M., and Kring, D. A. 2020. Earth's Impact Events through Geologic Time: A List of Recommended Ages for Terrestrial Impact Structures and Deposits. *Astrobiology* 20: 91–141.
Scholl, C. 2005. "The Influence of Multidimensional Structures on the Interpretation of LOTEM Data With One-Dimensional Models and the Application to Data From Israel." PhD thesis, University of Cologne. http://kups.ub.uni-koeln.de/id/eprint/1597.
Senut, B., and Ségalen, L. 2014. Neogene Palaeoenvironments of the Namib Desert: A Brief Synthesis. *Transactions of the Royal Society of South Africa* 69: 205–211. https://doi.org/10.1080/0035919X.2014.958605.
Simpson, F., and Bahr, K. 2005. *Practical Magnetotellurics*. Cambridge, UK: Cambridge University Press.
Spies, B. R. 1989. Depth of Investigation in Electromagnetic Sounding Methods. *Geophysics* 54: 872–888. https://doi.org/10.1190/1.1442716.
Thomas, R. J., Macey, P. H., Spencer, C., Dhansay, T., Diener, J. F., Lambert, C. W., Frei, D., and Nguno, A. 2016. The Sperrgebiet Domain, Aurus Mountains, SW Namibia: A ~2020–850Ma Window Within the Pan-African Gariep Orogen. *Precambrian Research* 286: 35–58. https://doi.org/10.1016/j.precamres.2016.09.023.
Ugalde, H., Valenzuela, M., and Milkereit, B. 2007. An Integrated Geophysical and Geological Study of the Monturaqui Impact Crater, Chile. *Meteoritics and Planetary Science* 42: 2153–63. https://doi.org/10.1111/j.1945-5100.2007.tb01015.x.
Unsworth, M., Campos Enriquez, J., Belmonte, S., Arzate-Flores, J., and Bedrosian, P. 2002. Crustal Structure of the Chicxulub Impact Crater Imaged with Magnetotelluric Exploration. *Geophysical Research Letters* 29:35-1–35-4. https://doi.org/10.1029/2002GL014998.
Urbini, S., Nicolosi, I., Zeoli, A., El Khrepy, S., Lethy, A., Hafez, M., El Gabry, M., et al. 2012. Geological and Geophysical Investigation of Kamil Crater, Egypt. *Meteoritics & Planetary Science* 47: 1842–68. https://doi.org/10.1111/maps.12023.
Waxman, M. H., and Smits, L. 1968. Electrical Conductivities in Oil-Bearing Shaly Sands. *Society of Petroleum Engineers Journal* 8: 107–122. https://doi.org/10.2118/1863-A.
Winsauer, W. O., and McCardell, W. M. 1953. Ionic Double-Layer Conductivity in Reservoir Rock. *Journal of Petroleum Technology* 5: 129–134. https://doi.org/10.2118/953129-G.
Yee, K. 1966. Numerical Solution of Initial Boundary Value Problems Involving Maxwell's Equations in Isotropic Media. *IEEE Transactions on Antennas and Propagation* 14: 302–7. https://doi.org/10.1109/TAP.1966.1138693.
Yogeshwar, P. 2014. "A Resistivity-Depth Model of the Central Azarq Basin Area, Jordan: 2D Forward and Inverse Modeling of Time Domain Electromagnetic Data." PhD thesis, University of Cologne. http://kups.ub.uni-koeln.de/id/eprint/5713.
Yogeshwar, P., and Tezkan, B. 2017. Two-Dimensional Basement Modeling of Central Loop Transient Electromagnetic Data from the Central Azraq Basin Area, Jordan. *Journal of Applied Geophysics* 136: 198–210. https://doi.org/10.1016/j.jappgeo.2016.11.001.
Zhang, B., Qu, K., Yin, C., Wang, Y., Liu, Y., Ren, X., and Su, Y. 2025. Review of 3D Electromagnetic Modeling and Inversion for Mineral Exploration. *Geophysics* 90: WA47–WA59. https://doi.org/10.1190/geo2024-0132.1.
Zonge. 2000. *ZT-30 ZeroTEM Transmitter Manual*. http://www.zonge.com/legacy/PDF_TxManuals/Zt-30_man.pdf.